Electronic Supplementary Information

Engineering novel surface electronic states via complex supramolecular tessellaitons

Wenqi Hu[1,2,†], Mohammad A. Kher-Elden[3,†], Hexu Zhang [1,2] , Peng Cheng[1,2], Lan Chen[1,2,5], Ignacio Piquero-Zulaica[4], Zakaria M. Abd El-Fattah[3,*], Johannes V. Barth[4], Kehui Wu[1,2,5*] and Yi-Qi Zhang[1,5*]

[1]Institute of Physics, Chinese Academy of Sciences, Beijing 100190, China.

[2]School of Physical Sciences, University of Chinese Academy of Sciences, Beijing 100049, China.

[3]Physics Department, Faculty of Science, Al-Azhar University, Nasr City E-11884 Cairo, Egypt.

[4]Physics Department E20, Technical University of Munich, D-85748 Garching, Germany.

[5]Songshan Lake Materials Laboratory, Dongguan, Guangdong 523808, China.

†These authors contributed equally to this work.

Corresponding Authors

*E-mail: z.m.abdelfattah@azhar.edu.eg

*E-mail: khwu@iphy.ac.cn

*E-mail: yiqi.zhang@iphy.ac.cn

Index

Approximation of the nanopore sizes in three supramolecular phases

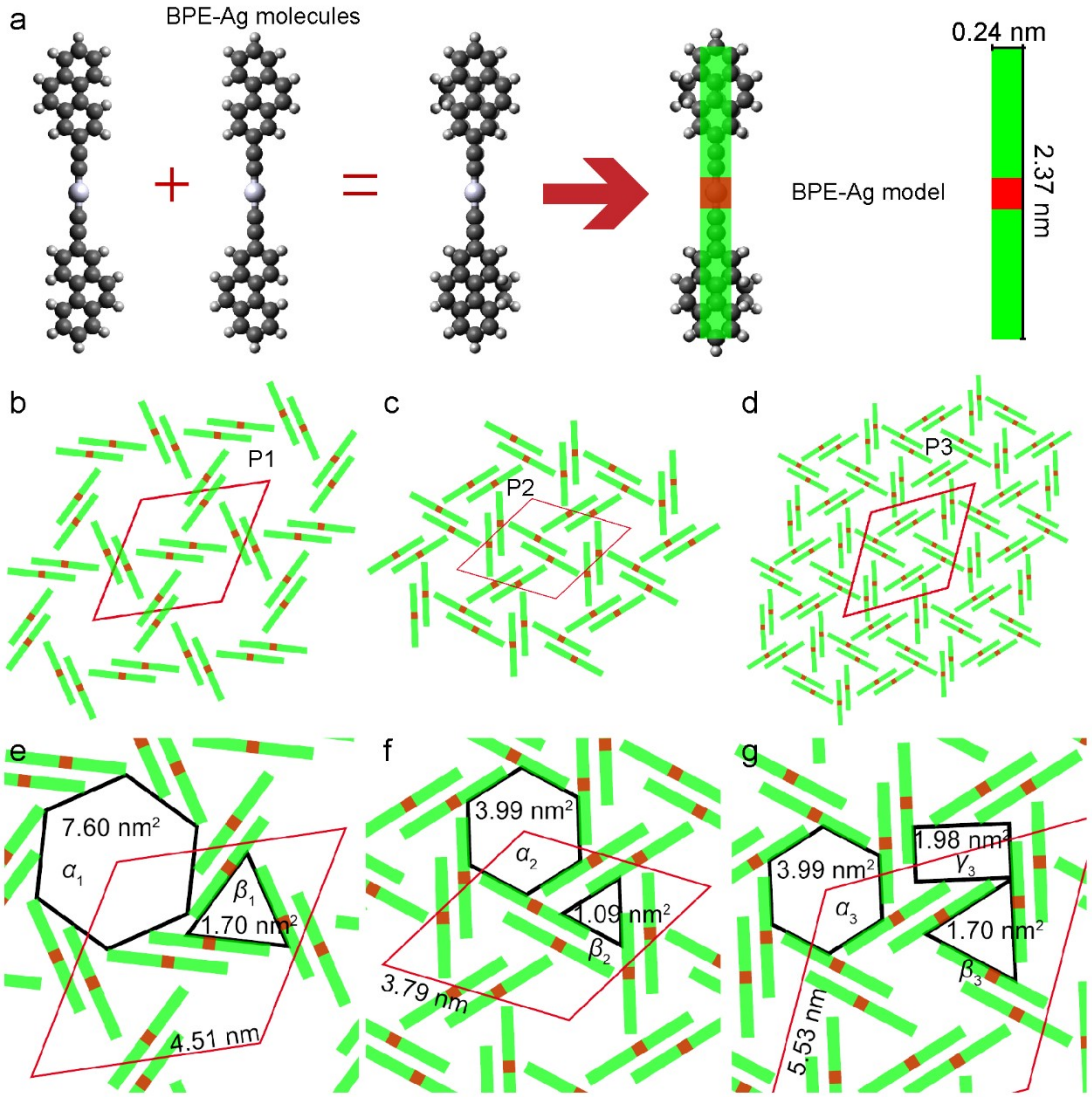

Figure S1. (a) Abstracting the dimension of a BPE-Ag complex via DFT calculated molecular models. (b-d) New representations of three phases using abstracted BPE-Ag model. (e-g) The estimated sizes of various types of atypical pores in three phases. Red rhombus indicates the unit cell in each phase with its dimension indicated.

Approximation of the BPE-Ag complex dimension: The organometallic BPE-Ag complexes present two configurations in all three networks[1]. Therefore, the gas-phase structure of *trans* and *cis* conformers were firstly relaxed using ORCA quantum chemistry code[1, 2] and were superimposed to have a mirror symmetric structure, from which a bar-shaped model can be abstracted (Fig. S1a). The long side of green rectangle was 2.37 nm, defined as the C-C distance between two outermost carbon atoms and

short side was 0.24 nm, defined as the C-C distance within the benzene ring. The red square (0.24 nm × 0.24 nm) highlights the alkynyl-Ag atom.

The new representations of the three phases: The STM image of each phase was superimposed with rectangular bars, which are arranged in accordance with the BPE-Ag complexes to achieve the best fit. A parallel configuration of two paired rectangular (mimic the BEP-Ag dimer) was enforced. Importantly, the red square in the green bar matches the alkynyl-Ag atom such that the paired the rectangular bars follow the same registry of the BPE-Ag pairs[1]. The new representations of three types of porous phases are illustrated by Fig. S1b-d and the unit cells of three phases agree well with the experimental data.

Calculation of different pore sizes in three phases: Nanopores with atypical shapes were denoted by α_i, β_i and γ_i wherein i distinguish three phases (cf. Fig. S1e-g). For α_i and β_i pores, we define the confined area by fitting a regular hexagon and a triangle with maximum area for all phases. The area of γ_3 is defined by that of the largest rectangle suitable for the pore. The obtained nanopore sizes are indicated in the Fig. S1e-g.

EPWE paired dumbbells model and the potential landscape of the three networks

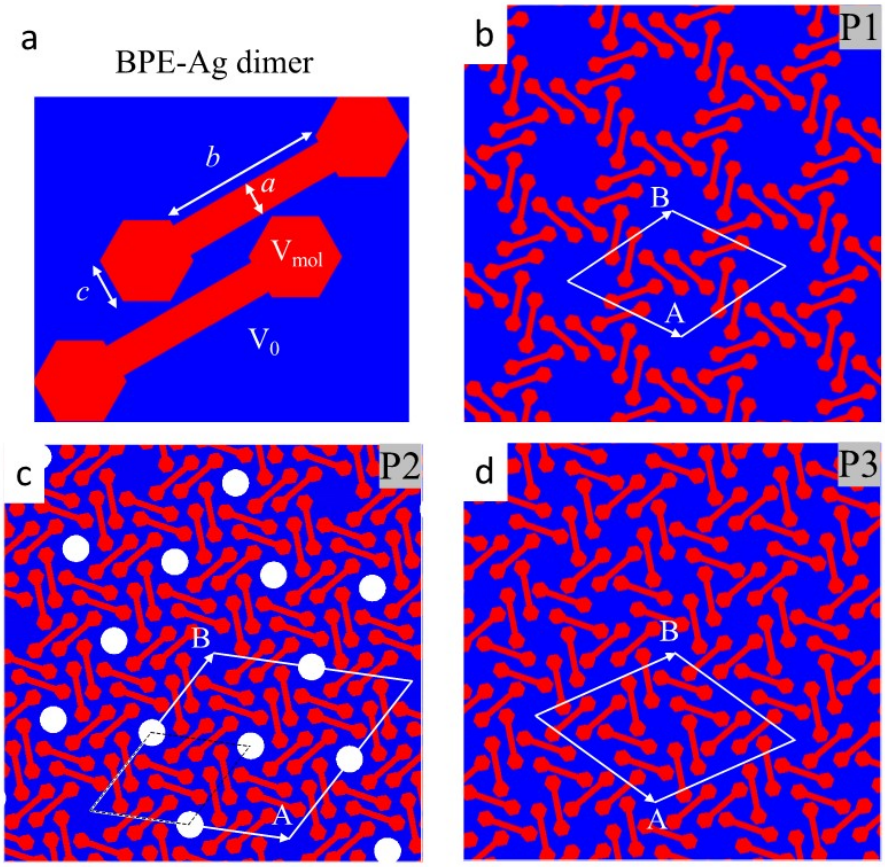

Figure S2. (a) Abstraction of the BPE-Ag dimer as paired dumbbells with dimensions ($a \sim 2.4$ Å, $b \sim 11.8$ Å, and $c = 3.3$ Å) consistent with the real geometry in Fig. S1. The potential inside these dimers (red) is set to $V_{mol} = 800$ meV and to $V_0 = 0$ for the substrate (blue). Six such dimers placed at a distance from the pore center and mutually rotated 60 degrees, defines the experimental pore size, and when translated with the lattice vectors $\boldsymbol{A} = \boldsymbol{B}$ yield the three phases in (b-d). The white lines and arrows in (b-d) define the unit cell area and vectors, respectively. These $A = B \sim 45.13$ Å (P1), $A = B \sim 75.78$ Å (P2), and $A = B \sim 56.80$ Å (P3). Note that for P2 phase filled pores are also present (white circles of $V = 220$ meV), so that the unit cell vectors of P2 is twice as large the fully filled or empty lattice, leading to four times larger unit cell (black dashed lines in (c)). For optimal fitting of the experimental data, the relative positions between dimers were slight relaxed within ~ 1 Å. For the P1 and P2 phases the experimental periodicity is preserved, while for the P3 phase this was enlarged by a small factor of ~ 1.026 for optimized fitting.

Experimental d*I*/d*V* spectroscopic data compared with EPWE simulations for P1

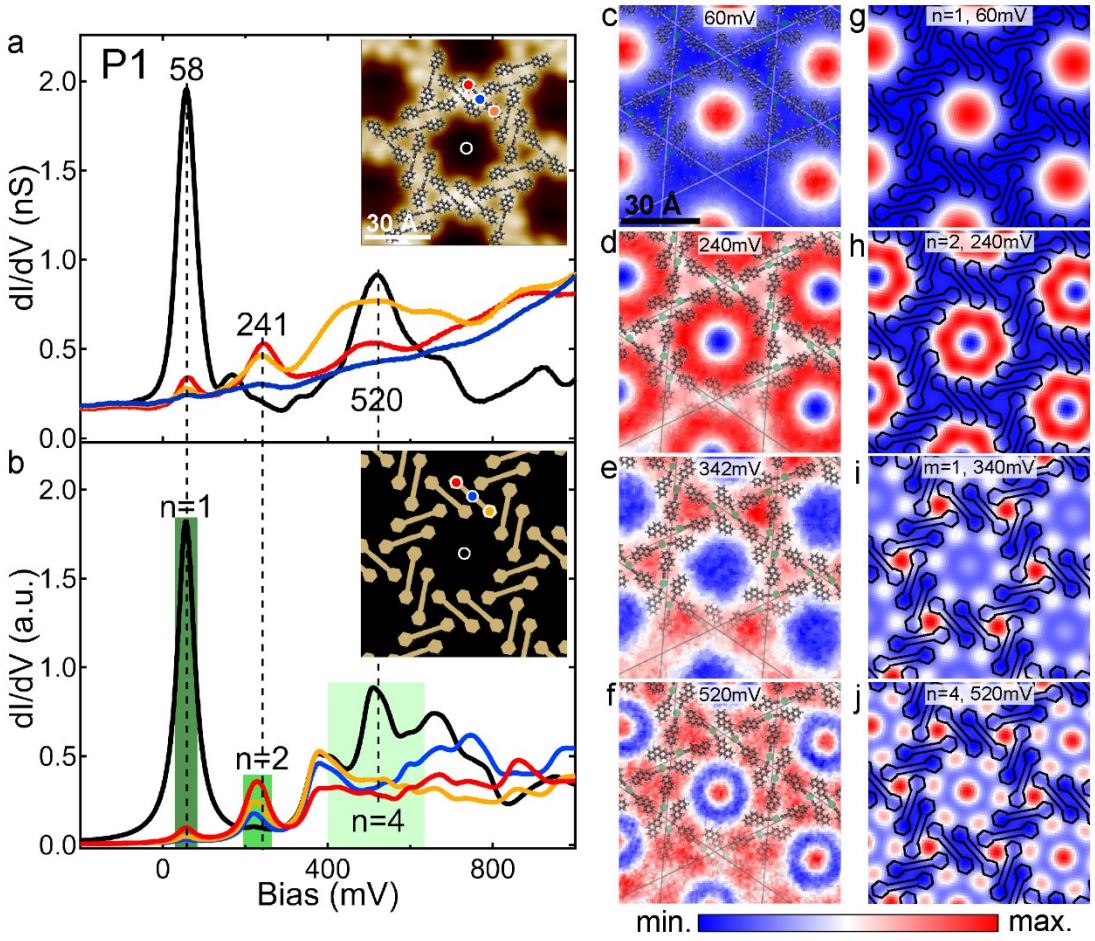

Figure S3. (a) Experimental site-dependent d*I*/d*V* spectra of the P1 phase. Inset: high-resolution STM image of P1 superimposed with BPE-Ag models. The spectra positions are specified. Set point: I_t = 30 pA; U_b = - 200 mV; U_m = 20 mV. (b) EPWE simulated site-dependent LDOS curves of P1. The inset depicts the 2D potential (cf. Fig. S2b). (c-f) Measured d*I*/d*V* maps of P1 phase at different bias voltages, superimposed with BPE-Ag models. Set point: I_t = 30 pA, U_m = 20 mV; U_b = 240 mV in (c, d), 467 mV in (e), and 655 mV in (f). Tiling of P1 is highlighted. (g-j) EPWE simulated LDOS maps at corresponding energies.

To avoid redundancy, spectroscopic features of P1 already discussed in the main text will not be present in the followings and same scheme is applied to the description of the other two phases. The STS spectrum taken above EP molecule close to β_1 (cf. orange point in the inset of Fig. S3a) also shows two resonances at 58 mV and 241 mV

with identical energy positions but slightly low intensity compared to those in the red curve. Notably, the orange curve presents a much prominent broad feature in energy range between 300 to 730 mV.

For the dI/dV map measured at V_B = 342 mV, the intensity in β_1 is most prominent which is in contrast to the minimum amplitude presented in α_1 (Fig. S3e). The LDOS map at this energy is coherent with the point spectra that the dI/dV signal is higher on the EP molecule close to β_1 (orange curve in Fig. S3a). Interestingly, the LDOS pattern in β_1 also shows a triangular shape, which rotates clockwise ~ 49 degrees away from the triangular tile, giving rise to a cyclically arranged chiral pattern (Fig. S6a). At 520 mV, the LDOS at the center of α_1 exhibits a local maximum whereas for β_1, a central maximum extends to the surface underneath the phenanthrene backbone (Fig. S3f), forming a three-winged propeller shape with handedness[3] (cf. also Fig. S6b).

EPWE simulations of the P1 phase reproduces the resonance positions (n = 1, 2 and 4) as well as the shape of three site-dependent STS curves (cf. Fig. S3a and b). In the simulated LDOS map at 340 mV, the maximum intensity appearing in the β_1 pores was captured (Fig. S3e and i) and it can be understood as the lowest confined state (m = 1) for the triangular pore. However, the simulated LDOS map at 520 meV (Fig. S3f) deviates slightly from the experimental data as the propeller-shaped LDOS in β_1 (non-negligible intensity beneath the phenanthrene backbone) is not reproduced and the simulated 6-fold flower-like pattern in the corners of α_1 (Fig. S3j) was not observed. These discrepancies are presumably ascribed to that molecular states or molecule-surface hybridization is not accounted in the EPWE calculation.

Experimental d*I*/d*V* spectroscopic data compared with EPWE simulations for P2

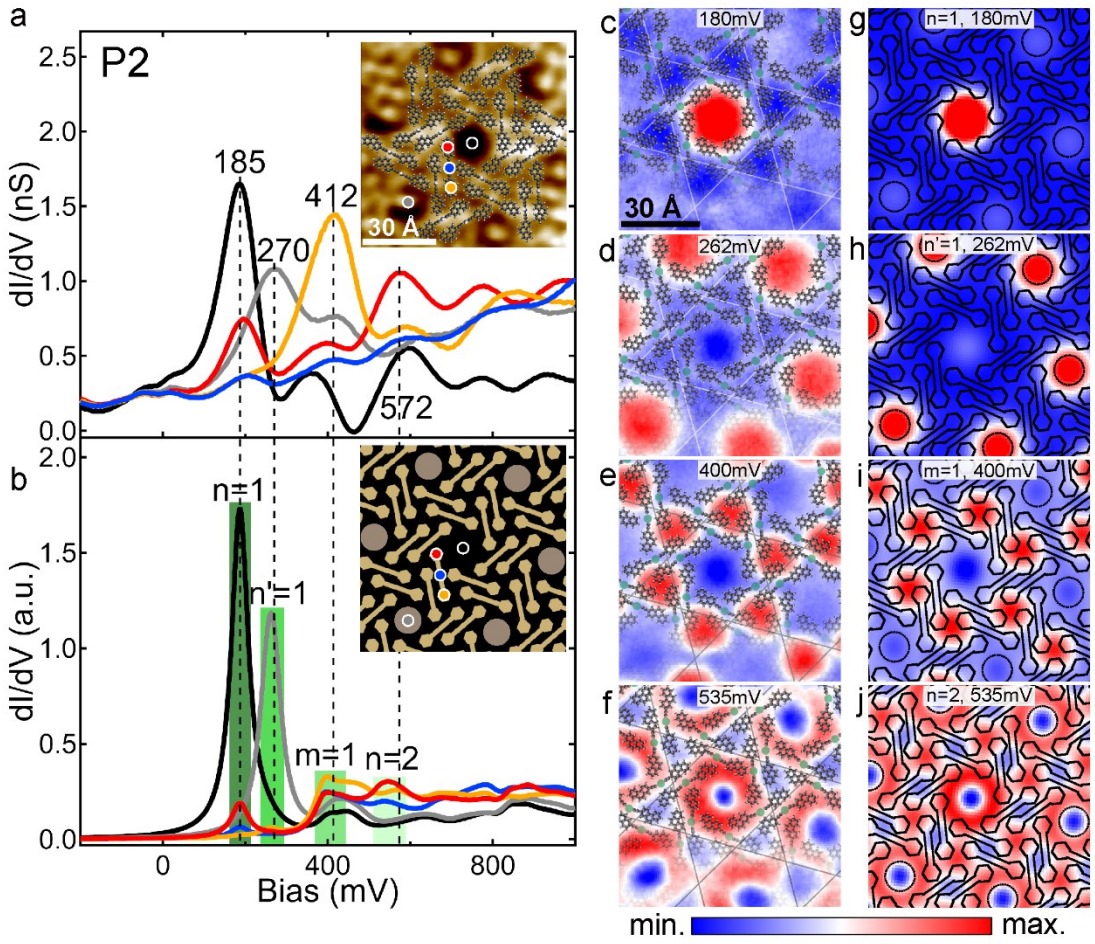

Figure S4. (a) Experimental site-dependent d*I*/d*V* spectra of the P2 phase. Inset: high-resolution STM image of P2 superimposed with BPE-Ag models with specified spectra positions. Set point: I_t = 30 pA; U_b = - 200 mV; U_m = 20 mV. (b) EPWE simulated site-dependent LDOS spectra of P2 (cf. Fig. S2c). (c-f) Measured d*I*/d*V* maps of the P2 phase at different bias voltages, superimposed with BPE-Ag models. Set point: I_t = 50 pA, U_m = 8 mV; U_b = 400 mV in (c-e) and 656 mV in (f). Tiling of P2 is highlighted. (g-j) EPWE simulated LDOS maps at corresponding energies.

Three site-dependent d*I*/d*V* curves acquired on the BPE-Ag in the P2 phase are displayed in Fig. S4a. The spectrum taken at the empty α_2 centre shows three main resonance peaks at V_B = 185 mV (n = 1), 361 mV and 598 mV (close to n = 2), followed by another two small bumps at higher bias (cf. black curve in Fig. S4a). The spectrum taken above filled α_2 (cf. grey line in Fig. S4a) show a systematic shift of the three main

peak positions towards higher bias: 270 mV (n' = 1), 412 mV and 617 mV (n' = 2). The STS spectra taken on the BPE-Ag species, namely at phenanthrene backbones and alkynyl-Ag atom, share similar resonance peak positions (cf. red, orange and blue curves in Fig. S4a) with different height distribution varied with bias voltages. For the red curve, as its position is close to α_2, the first two confined state (n = 1 and 2) are reflected at the prominent resonance peak positions at 195 mV and 572 mV as well as in its corresponding dI/dV maps (cf. Fig. S4c and f). For the yellow curve depicted in Fig. S4a, the resonance peak at 412 mV has the highest intensity, which corresponds to the first confined state (m = 1) in the β_2 pore. The energy position of the m = 1 resonance state coincides with the peak (361 mV) at the empty α_2 centre and the peak (412 mV) at filled α_2. At the same energy, STS mapping shows indeed high LDOS intensity in β_2, which smears out, extending to the area underneath the EP backbones (Fig. S4e), and forms triangular-shaped pattern with chiral organization (cf. Fig. S6c).

For EPWE simulated STS spectra, not only the adsorbate-induced energy shift of α_2 pore has been reproduced, but also the characteristic peak positions as well as their relative intensity of the red and yellow curves on the molecular sites. Similar to P1, a steady increasing in the STS background contributed at the molecular state is not reflected in the EPWE modelling. For V_B = 400 mV (m = 1), the simulated LDOS map captures the large electron density distribution in β_2 pores, which extends towards to the area beneath the surrounding EP molecules (Fig. S4e and i). Moreover, the faint intensity at filled α_1 pores and diminished LDOS at empty α_1 are all reproduced. At 535 mV (close to n = 2), the model nicely captures the donut-shaped LDOS at α_2 pores. Note that the LDOS intensity in empty α_2 slightly surpass that in filled neighbours (Fig. S4f and j). The minor inconsistency is that m = 1 state diminishes at 535 mV in the experimental data, whereas its finite magnitude still presents in the simulated LDOS map (Fig. S4f and j).

Experimental d*I*/d*V* spectroscopic data compared with EPWE simulations for P3

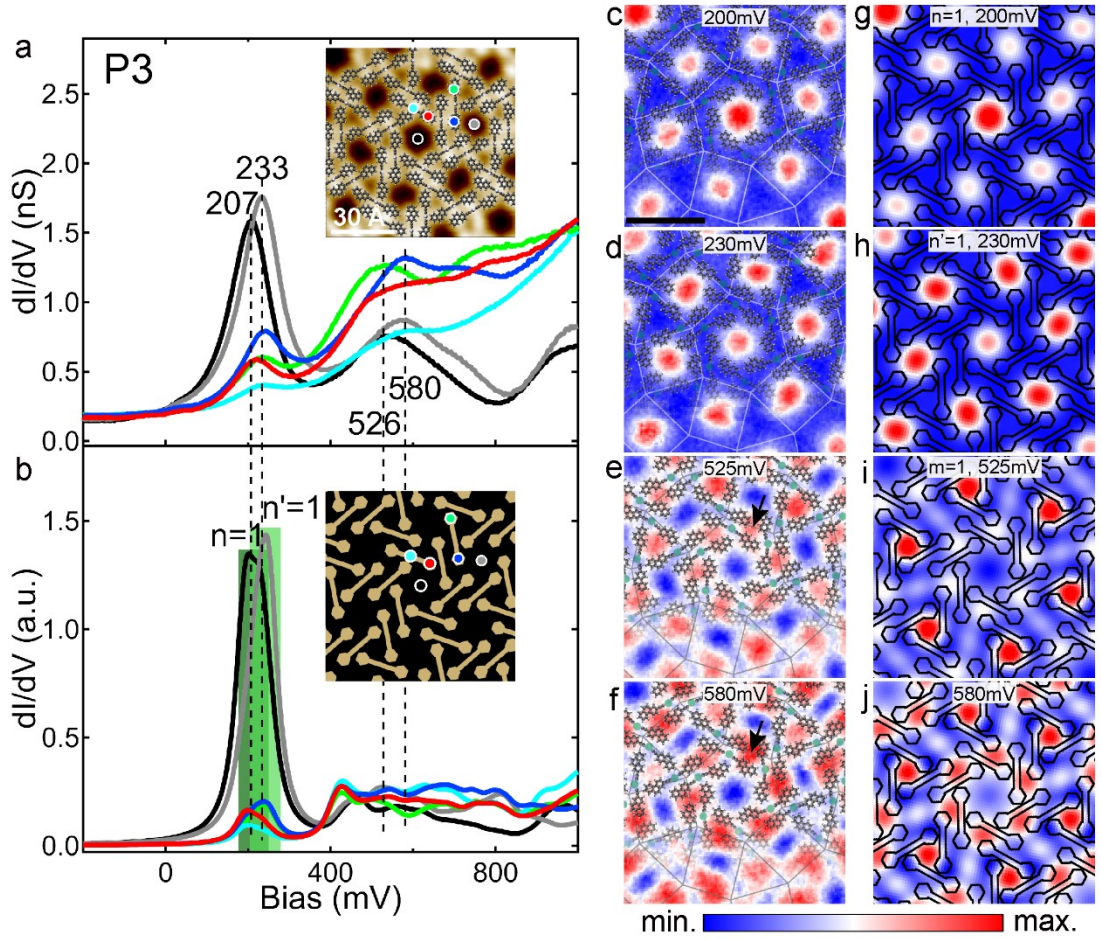

Figure S5. (a) Experimental site-dependent d*I*/d*V* spectra of the P3 phase. Inset depicts high-resolution STM image of P3 superimposed with BPE-Ag models and spectroscopic positions. Set point: I_t = 30 pA, U_b = - 200 mV; U_m = 20 mV. (b) EPWE simulated site-dependent LDOS spectra of P3. Inset: EPWE potential landscape (cf. Fig. S2d). (c-f) Measured d*I*/d*V* maps of P3 phase at different bias voltages, superimposed with BPE-Ag models. Arrows in (e, f) indicate the finite area between α_3 and γ_3. Set point: I_t = 30 pA, U_m = 20 mV; U_b = 500 mV in (c), 550 mV in (d), 525 mV in (e), and 580 mV in (f). Tiling of P3 is highlighted. Scale bars in all measured d*I*/d*V* maps: 30 Å. (g-j) EPWE simulated LDOS maps of P3 phase.

Site-dependent d*I*/d*V* spectra taken on the BPE-Ag in the P3 phase are displayed in Fig. S5a. The spectrum taken in the α_3 pore shows two main peaks at 207 mV (n = 1) and 544 mV, respectively. (cf. the black curve in Fig. S5a). The shape of the d*I*/d*V*

curve recorded inside the γ_3 pore is almost identical to that of α_3 with an energy upshift about 26 meV (cf. grey curves in Fig. S5a). For the spectrum taken on the EP molecule close to the α_3 pore (red point), the first resonance peak occurs at 220mV and a broad shoulder at around 526 mV (cf. red curve in Fig. S5a). The green curve in Fig. S5a was taken on the EP molecule locating in between β_3 and γ_3. Its first resonance appears at 234 mV, similar to that of the grey curve. Its second peak position coincides with that of the black curve (526 mV), yet with much higher intensity. At this energy, STS map reveals that the LDOS in β_3 reaches a maximum (m = 1), whereas the LDOS in α_3 and γ_3 shows a minimum (Fig. S5e). Moreover, the small area enclosed by three EP molecules in between α_3 and γ_3 also present finite LDOS intensity (indicated by an arrow in Fig. S5e). For the dI/dV spectrum taken on the EP molecule close to the γ_3 pore (blue point), the positions of its first and second resonances are the same as that of the grey curve (Fig. S5a). The dI/dV map at 580 mV shows that the electron density in β_3 is less prominent than that in the finite area between α_3 and γ_3 (cf. arrow in Fig. S5f), wherein the LDOS also displays organizational chirality[3] (cf. Fig. S6d). The dI/dV spectrum recorded on the alkynyl-Ag atom show weak bump features at 233 mV and 544 mV with a rising background (cf. light blue curve in Fig. S5a).

EPWE simulated LDOS maps at two higher bias values agree quite well with the experimental data, apart from some minor inconsistency: (i) at 525 mV, finite intensity of n' =1 state still exists (Fig. S5i); (ii) at 580 mV, the simulated intensity of the central six-fold pattern is slightly weaker than that in the β_3 pore (Fig. S5j), which is opposite to the experimental LDOS character (Fig. S5f). These two discrepancies can also be recognized in the simulated dI/dV curves (Fig. S5b) that an increasing DOS background at the molecular sites are not captures, which could be presumably ascribed to the missing molecular states information in the EPWE calculation.

Organizational chirality present in the confined electronic density

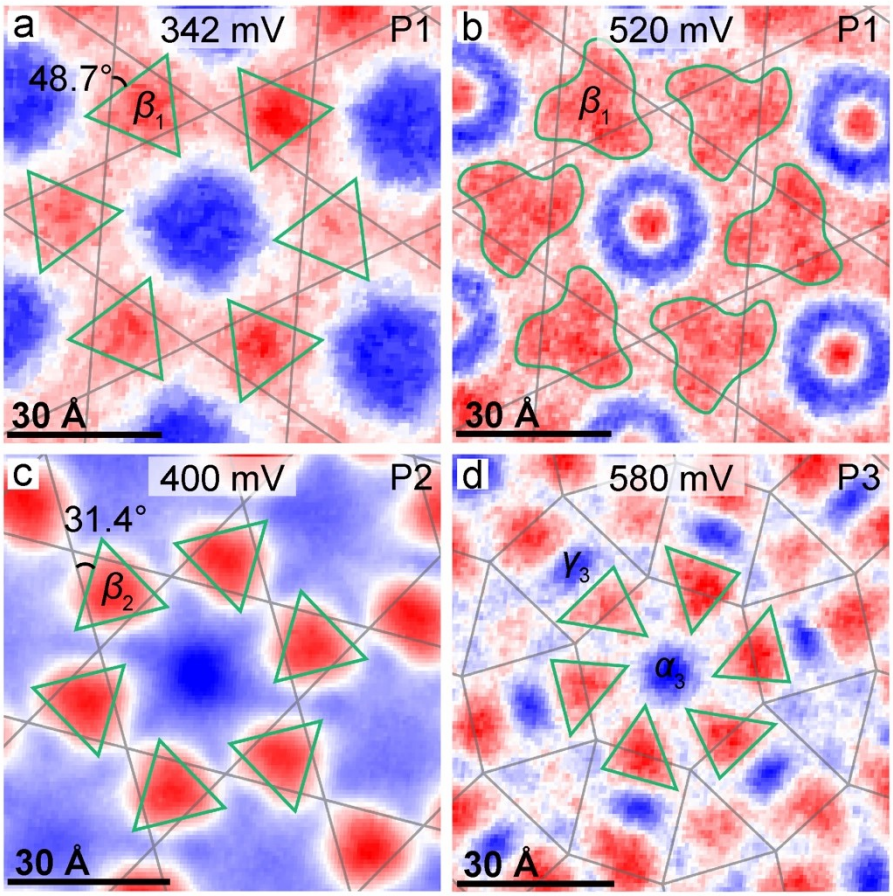

Figure S6. (a) At 342 mV, the LDOS pattern in β_1 presents a triangular shape, which rotates 48.7 degrees clockwise with respect to the host triangular tile, leading to a cyclic chiral arrangement around the hexagonal tile. (b) At 520 mV, the LDOS pattern of β_1 converts into a three-winged propeller shape with handedness. (c) At 400 mV, the LDOS pattern in β_2 shows a triangle-like shape, which rotates 31.4 degrees clockwise with respect to the hosting triangular tile, bestowing an organizational chirality into the LDOS pattern. (d) A local irregular triangular-shaped LDOS exhibits at the boarders between α_3 and γ_3 at 580 mV and six of them circling the hexagonal tile present organizational chirality. Black lines highlight tilings of the three phases.

Effective α_1 pore size analysis using a quantum particle-in-a-box model

Table 1. For the three low-lying confined states of α_1 ore of the P1 phase, the columns denote the number, the normalized eigenvalues λ_n/m^*, the energy $E_n(D_{\text{real}})$ assuming a distance D_{real}, the energy $E_n(D_{\text{eff}})$ assuming distance D_{eff} and the experimental energy E_n (Exp).

Number	λ_n/m^* (meV * nm^2)	$E_n(D_{\text{real}})$ (meV)	$E_n(D_{\text{eff}})$ (meV)	E_n (Exp) (meV)
$n = 1$	1432.2	121.8	47.3	58
$n = 2$	3623.8	410.6	224.3	240
$n = 4$	7497.2	923.1	533.5	520

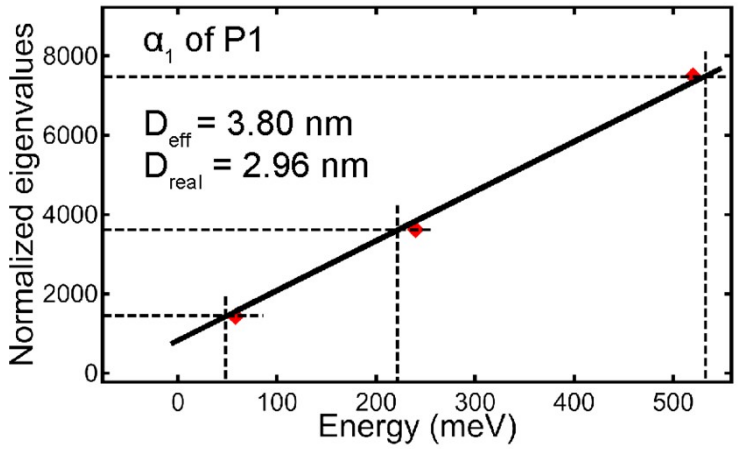

Figure S7. Obtaining effective distance of α_1 of P1 using a particle-in-a-box model. Red rhombuses highlight the normalized eigenvalues versus the experimental confined state energies E_n (Exp) for the P1 phase. The black line is the fitting curve.

To evaluate the effective size of the α_1 pore, we employ a previously reported analysis via comparing it to a quantum particle in a 2D hexagonal box[4, 5]. The eigenstate energies E_n can be calculated by $E_n = E_0 + \frac{\lambda_n}{m^* \Omega}, n = 1, 2, 3...$, where E_0 is the onset energy of Ag(111) surface state, m^* is the effective mass[6, 7] and the eigenvalues λ_n can be numerically obtained for the hexagonal box[5, 8]. The area of the hexagon $\Omega = \sqrt{3}/2D^2$, where D is the distance between parallel hexagon sides. According to our EPWE model,

the $m^* = 0.455\ m_e$ is kept the same for three phases and the Ag(111) surface state onset energies for matching STS data with EPWE simulations are E_0 = -70 meV (cf. Methods). We can rewrite the eigenstate energies equation: $\frac{\lambda_n}{m^*} = \frac{\sqrt{3}}{2} D^2 (E_n - E_0)$, to extract the effective diameter D_{eff}. According the early reports,[4, 9] we can calculate the normalized eigenvalues λ_n/m^* for our hexagonal nanopores (cf. Table 1). Following the analysis shown in Figure S1, we can obtain the distance (D_{real} = 2.96 nm, cf. Fig. S7) between parallel hexagon sides of α_1. Comparing the D_{real} and the effective diameter D_{eff} obtained by fitting the experimental eigenstate energies, we found that an effective diameter D_{eff} (3.80 nm) is larger than the model. Therefore, our analysis indicates that the α_1-QDs are intercoupled.

Randomly filling of α_2 nanopores in P2 with trapped molecules

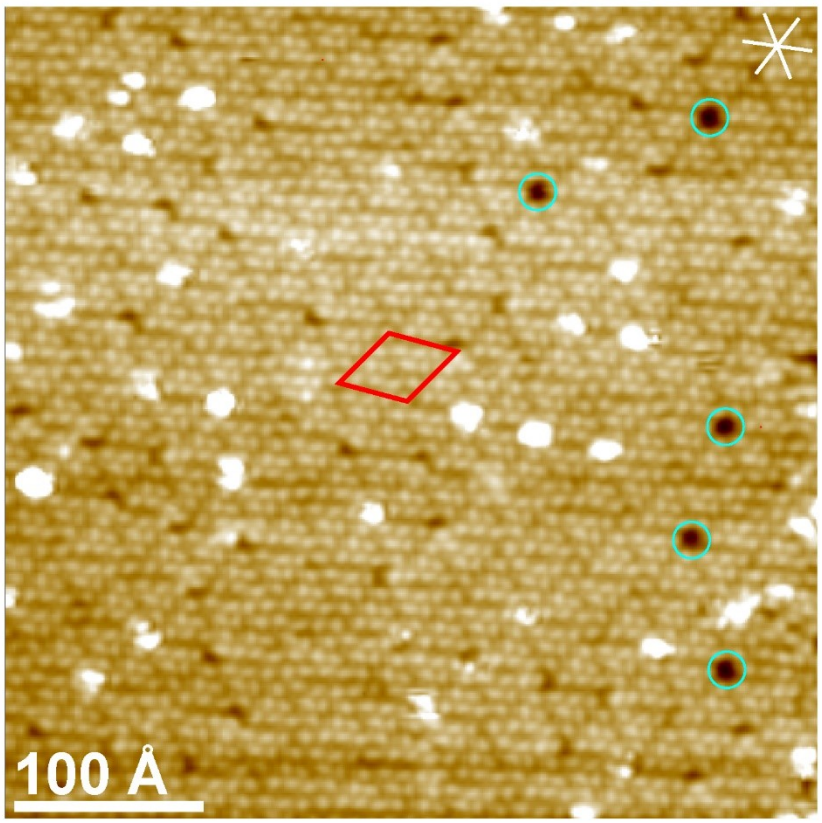

Figure S8. Large-scale STM image of the P2 phase grown on Ag(111)/mica. Scanning parameters: I_t = 50 pA, U_b = 1.0 V. Red rhombus indicates the unit cell. Cyan cycles highlight hexagonal nanopores without guest molecules. High-symmetry directions of the Ag(111)/mica surface are indicated by white lines. It is clear to see that the distribution of filled α_2 pores is disordered.

Identifying the guest molecule in the nanopore of the P2 phase

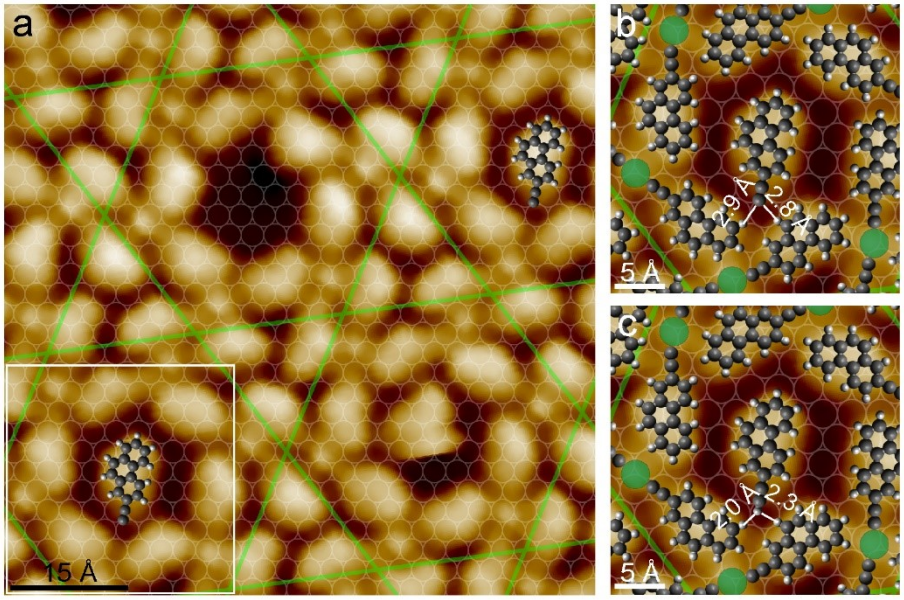

Figure S9. (a) High-resolution STM image of trapped molecular species in the P2 domain. (b,c) the same zoomed-in image of an area in (a) with scaled models superimposed. Note that deprotonated and intact EP models are assigned for the guest molecule in (b) and (c), respectively. Scanning parameter: I_t = 50 pA, U_b = 1.0 V.

A high-resolution STM image of the P2 domain is depicted in Figure S9 to show that some of the nanopores are occupied by single molecular species. The shape of the guest species mimics that of an EP molecule. However, it is unclear whether it is deprotonated or not. Therefore, using a similar strategy[1], BPE-Ag complexes with well-defined registry were firstly superimposed in a selected area. The guest molecule was modelled by DFT-calculated deprotonated (Fig. S9b) and intact EP molecule (Fig. S9c), respectively. Via modeling, it is found that the intact EP molecule exhibit rather short distances (2.0 and 2.3 Å, cf. white lines in Fig. S9c) between the terminal alkyne H atom and the H atoms from the adjacent phenanthrene backbones, which indicates a repulsive interaction[10]. On the contrary, when the trapped molecule is modeled by a deprotonated EP, the distances between the terminal alkynyl C atom and the adjacent H atoms are 2.8 and 2.9 Å (cf. white lines in Fig. S9b), which match the typical distances for the ionic hydrogen bond[11].

High-resolution STM images acquired together with the STS maps

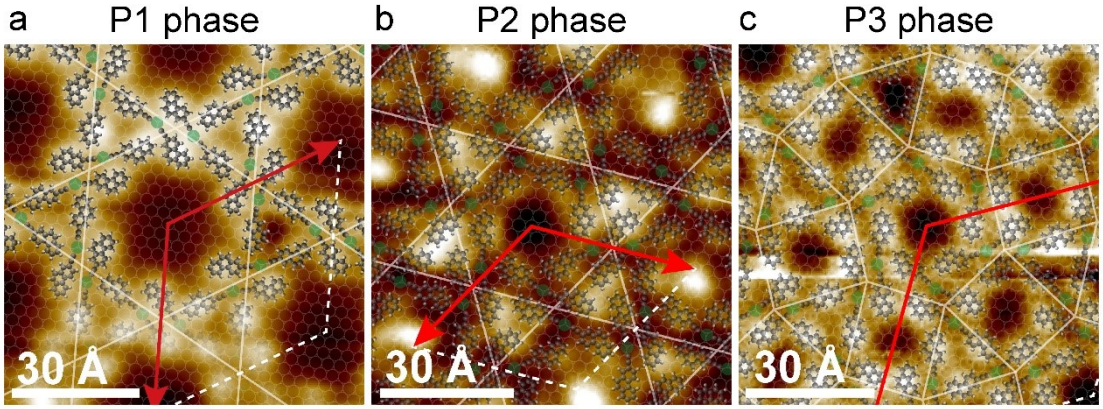

Figure S10. Molecular-level expression of three different porous phases: (a) phase P1, (b) phase P2, and (c) phase P3, with a commensurate unit cell model and proposed molecular registry. Those high-resolution STM images were acquired together with LDOS maps and the white lines highlight (3.6.3.6) and (3.4.6.4) Archimedean tilings. Scanning parameters for each image are: (a) I_t = 30 pA, U_b = 240 mV; (b) I_t = 50 pA, U_b = 400 mV; (c) I_t = 30 pA, U_b = 500 mV, respectively.

Tight-binding band structures for the P3 network for different hopping parameters among distinct pores

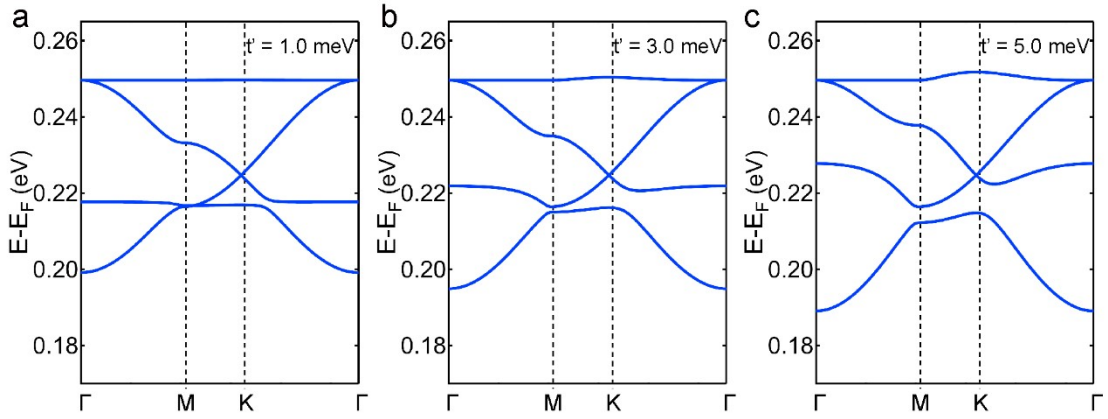

Figure S11. TB described band structures of P3 with (a) t' = 1.0 meV, (b) t' = 3.0 meV and (c) t' = 5.0 meV.

It is obvious that once the coupling between the α_3 and γ_3-QDs are switched on (t' > 0), an energy gap occurs promptly between the first and second band. Furthermore, the gap becomes larger with increasing t'.

Reference

1. W. Hu, H. Zhang, P. Cheng, L. Chen, Z. Chen, S. Klyatskaya, M. Ruben, J. V. Barth, K. Wu and Y.-Q. Zhang, *CrystEngComm*, 2021, **23**, 7822-7830.
2. F. Neese, *WIREs Comput. Mol. Sci*, 2012, **2**, 73-78.
3. F. Klappenberger, D. Kühne, W. Krenner, I. Silanes, A. Arnau, F. J. García de Abajo, S. Klyatskaya, M. Ruben and J. V. Barth, *Nano Lett.*, 2009, **9**, 3509-3514.
4. F. Klappenberger, D. Kühne, W. Krenner, I. Silanes, A. Arnau, F. J. García de Abajo, S. Klyatskaya, M. Ruben and J. V. Barth, *Phys. Rev. Lett.*, 2011, **106**, 026802.
5. J. Li, W. D. Schneider, S. Crampin and R. Berndt, *Surf. Sci.*, 1999, **422**, 95-106.
6. J. Li, W.-D. Schneider and R. Berndt, *Phys. Rev. B*, 1997, **56**, 7656-7659.
7. L. Bürgi, O. Jeandupeux, A. Hirstein, H. Brune and K. Kern, *Phys. Rev. Lett.*, 1998, **81**, 5370-5373.
8. E. Lijnen, L. F. Chibotaru and A. Ceulemans, *Phys. Rev. E*, 2008, **77**, 016702.
9. N. Kepčija, T.-J. Huang, F. Klappenberger and J. V. Barth, *J. Chem. Phys.*, 2015, **142**, 101931.
10. T. Steiner, *Angew. Chem. Int. Ed.*, 2002, **41**, 48-76.
11. Y.-Q. Zhang, J. Björk, P. Weber, R. Hellwig, K. Diller, A. C. Papageorgiou, S. C. Oh, S. Fischer, F. Allegretti, S. Klyatskaya, M. Ruben, J. V. Barth and F. Klappenberger, *J. Phys. Chem. C*, 2015, **119**, 9669-9679.